Compression behaviour of nitridocarbidosilicates $M_2[Si_4N_6C]$ M = Y, Ho, Er studied with X-ray diffraction and ab initio calculations

Alexandra Friedrich [a,*], Karsten Knorr [b,1], Björn Winkler [a], Alexandra Lieb [c,2], Henning A. Höppe [c,3], Wolfgang Schnick [c], Victor Milman [d], Michael Hanfland [e]

[a] Institut für Geowissenschaften, Abt. Kristallographie, Johann Wolfgang Goethe-Universität Frankfurt, Altenhöferallee 1, D-60438 Frankfurt am Main, Germany
[b] Institut für Geowissenschaften, Mineralogie/Kristallographie, Christian-Albrechts-Universität zu Kiel, Olshausenstr. 40, D-24098 Kiel, Germany
[c] Department Chemie und Biochemie, Lehrstuhl für Anorganische Festkörperchemie, Ludwig-Maximilians-Universität München, Butenandtstrasse 5-13 (D), D-81377 München, Germany
[d] Accelrys Inc., 334 Cambridge Science Park, Cambridge CB4 0WN, UK
[e] European Synchrotron Radiation Facility (ESRF), B.P. 220, F-38043 Grenoble Cedex, France

1. Introduction

Nitridocarbidosilicates are structurally related to incompressible compounds such as the binary nitride Si_3N_4 [1], or the more complex nitridosilicates, e.g. $MYb[Si_4N_7]$ with M = Ba, Sr [2]. They are potential candidates for high performance applications due to their high mechanical hardness, and their exceptional thermal and chemical stability. Furthermore, rare earth containing or doped nitrido- or oxonitridosilicates like $(Sr, Ba)_2Si_5N_8:Eu^{2+}$ [3] or $SrSi_2O_2N_2:Eu^{2+}$ [4] gained industrial application as luminescent materials in phosphor-converted (pc) LEDs.

Nitridocarbidosilicates offer the possibility to further investigate interatomic interactions along the Si–N and Si–C contacts. An understanding of these bonds is a prerequisite for the design of new ultrahard materials [5] and for the systematic extension of this exciting new class of materials. One method to better characterise bonds is to investigate their pressure-dependence, but only few *in situ* high-pressure studies of nitridosilicates and related compounds exist. Such studies may yield surprising results as has been shown in a study of Si_3N_4, which was found to transform to a new high-pressure polymorph at pressures above 15 GPa and temperatures exceeding 2000 K [1]. The hardness of this phase has been suggested to be comparable to that of the hardest known oxides [1]. More recently, high-pressure studies were performed on the nitridosilicate $SrYb[Si_4N_7]$ and the oxonitridoaluminosilicates (so called sialons) $MYb[Si_{4-x}Al_xO_xN_{7-x}]$ ($x = 2$; M = Sr, Ba) [6]. These compounds are stable at high pressures up to about 40 GPa. As these compounds are structurally related to the nitridocarbidosilicates $Ln_2[Si_4N_6C]$, Ln = lanthanides, it was of interest to study the anion and cation substitution effects on the compressibility and phase stability.

Here, $Y_2[Si_4N_6C]$ [7] and the lanthanide-containing compounds $Ln_2[Si_4N_6C]$ with Ln = Ho [8], Er are studied. The three compounds

* Corresponding author. Tel.: +49 69 79840114; fax: +49 69 79840109.
E-mail address: friedrich@kristall.uni-frankfurt.de (A. Friedrich).
[1] Present address: Bruker AXSGmbH, XRD Marketing, Östliche Rheinbrückenstraße 49, D-76187 Karlsruhe, Germany.
[2] Present address: University of Southampton, School of Chemistry, Lab. 2003, Highfield, Southampton SO17 1BJ, UK.
[3] Present address: Institut für anorganische und analytische Chemie, Lehrstuhl Festkörperchemie, Universität Freiburg, Alberstrasse 21, D-79104 Freiburg im Breisgau, Germany.

are isotypic, they are crystallizing in the monoclinic space group $P12_1/c1$, the cell parameters are about $a \approx 5.9$ Å, $b \approx 9.9$ Å, and $c \approx 11.9$ Å with the monoclinic angle being almost 120°. All atoms are located on the general position 4*e*. The two symmetrically non-equivalent Ln- or Y-ions are each coordinated to six N atoms in the form of distorted octahedra (Fig. 1). Since the ionic radii of the Ln-ions and Y are essentially the same (about 1.04 Å for sixfold coordination [9]) we do not expect a significant dependence of the high pressure behaviour on the composition. However, a possible influence of the 4*f* electrons of Ho and Er on the structural behaviour at high pressures could lead to a difference in the compression mechanism with respect to the Y-bearing compound.

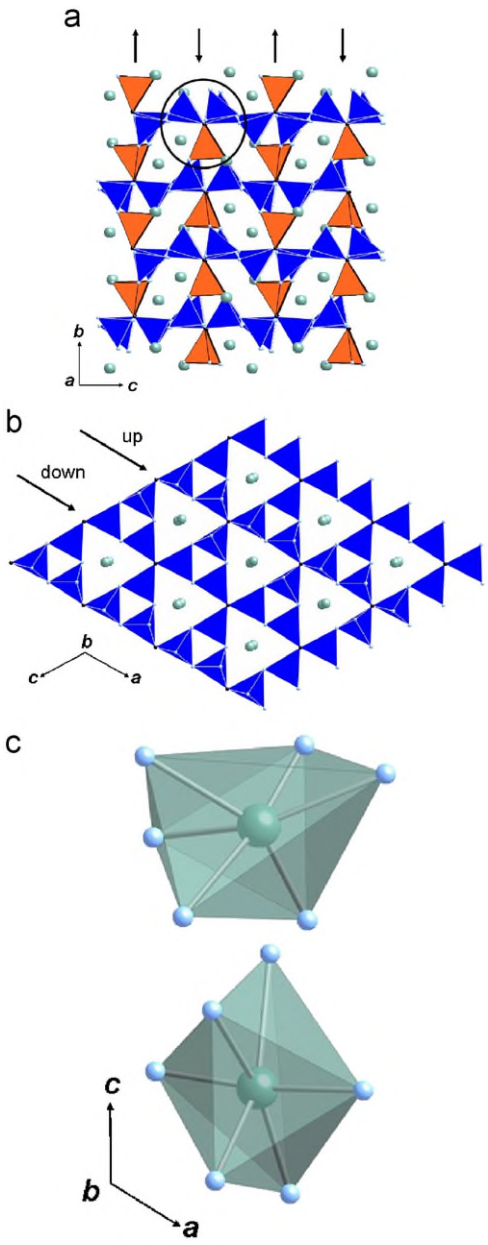

Fig. 1. (Colour online) Crystal structure of $Y_2[Si_4N_6C]$ at ambient pressure ($SiCN_3$ tetrahedra: orange/light grey and blue/dark grey, large spheres: yttrium, small blue/light grey spheres correspond to nitrogen and small black spheres to carbon). Panel (a) shows chains of star-like $C(SiN_3)_3$ units (encircled), running alternatingly oriented along *b* as indicated by the arrows; layers of $SiCN_3$-tetrahedra are corner connected in the monoclinic plane (b). These planes are stacked along *b* and connected via single-site $SiCN_3$-tetrahedra (orange/light grey) as shown in panel (a). Chains of star-like units having equal orientation are connected to layers in the *ab*-plane, which are alternatingly stacked along *c* (see up/down indicators in panel (b)). Panel (c) displays the two symmetrically inequivalent YN_6-polyhedra (top: Y_1N_6, bottom: Y_2N_6).

The structures of the title compounds can be described as a three-dimensional all-corner connected network of SiN_3C-tetrahedra (Fig. 1). The interesting feature in this framework are 'star-like units' $[C(SiN_3)_4]$ of four SiN_3C-tetrahedra sharing a common corner in the centre of the star-like unit. These units are therefore related to the $[N(SiN_3)_4]$ of four SiN_4-tetrahedra, which have been found in $M^{2+}Yb[Si_4N_7]$ [2]. While a structurally isotypic compound was found with composition $YBa[Co_4O_7]$ [10], no such structural units in oxosilicates have been reported up to now.

From a structural point of view, the nitridocarbidosilicates studied here differ from the hexagonal $MYb[Si_4N_7]$ compounds and from hexagonal $Ca_{0.8}Y_{1.2}Si_4N_{6.8}C_{0.2}$ [11] with respect to chains of the $[C^{[4]}(SiN_3^{[2]})_4]$-units that are stacked in an alternating way (Fig. 1). This leads to a reduction of the symmetry, from hexagonal to monoclinic [8]. The deviation of the monoclinic cell from the hexagonal system is small. The pseudohexagonal cell could also be described in a pseudo-orthorhombic setting in space group $P2_1/n$ with a $5.9 \times 9.9 \times 10.3$ Å^3 unit cell. While this setting would be the conventional choice, the pseudohexagonal cell is used throughout this work in order to facilitate a comparison with the structurally related $BaYb[Si_4N_7]$ (space group $P6_3mc$; $a \approx 6$ Å, $c \approx 9.8$ Å) [2]. The structure chosen here relates the monoclinic *a*, *b* and *c* axes of $Ln_2[Si_4N_6C]$ to the hexagonal *a* and *c* axes and a doubled hexagonal *a* axis of $BaYb[Si_4N_7]$. The monoclinic β angle then corresponds to the hexagonal γ angle of 120°.

Here, *in situ* high pressure powder X-ray diffraction and parameter free atomistic quantum mechanical modelling results are presented. With the latter, it would have been difficult to predict structural phase transitions, but in contrast to the high pressure powder diffraction studies, they give reliable information of pressure-induced changes of the atomic positional parameters.

2. Experimental

2.1. Synthesis

$Er_2[Si_4N_6C]$ was synthesized in analogy to the procedure reported for $Ho_2[Si_4N_6C]$ [8]. The X-ray phase analysis of both samples revealed impurities of the trigonal oxonitridosilicates $Ho_6[Si_{11}N_{20}]O$ and $Er_6[Si_{11}N_{20}]O$ [12]. However, as they were present in only very small amounts, they could not be included in the data treatment.

2.2. Powder X-ray diffraction

The $Ho_2[Si_4N_6C]$ and $Er_2[Si_4N_6C]$ powder samples were investigated at the ESRF at high pressures of up to 36 and 21 GPa, respectively, using a LeToullec diamond anvil cell. Neon was loaded as the pressure-transmitting medium using an autoclave. Holes serving as sample chamber (150 μm in diameter) were drilled through gaskets made of stainless steel (pre-indented to a thickness of 40 μm) using a spark-erosion drilling machine. Pressure was determined before and after each exposure by means of the ruby-fluorescence technique, applying the pressure scale of Mao [13]. *In situ* high-pressure synchrotron X-ray powder diffraction data were collected at station ID09A at a wavelength of 0.4138 Å using a MAR345 online image-plate scanner. The wavelength, the zero point of the image-plate scanner and the sample-to-detector distance of 362 mm were determined from a Si-reference sample. Diffraction data were collected up to a maximum $\sin\theta/\lambda$ of 0.502 Å^{-1}.

The diffraction images were processed and integrated using FIT2D [14]. Individual single diffraction spots from the sample and the pressure medium were masked manually and excluded from the integration. As the zero point of the image-plate scanner was off by 0.1 to 0.2 mm (1 to 2 pixel), the distortion of the diffraction images by the scanner was corrected using DatLab [15]. Cell parameters were refined from full profile fits with the General Structure Analysis System (GSAS) [16]. Due to the strong reflection overlap caused by the pseudo-symmetry of the monoclinic cell, the intensities of the powder peaks were constrained using the crystal structure data obtained from DFT calculations on the isotypic Y-compound. The refinement of the crystal structure was not possible unambiguously due to the limited resolution and data range, and the complexity of the crystal structure. Representative examples of two profile fits and their respective difference plots are shown in Fig. 2.

2.3. Ab-initio calculations

Currently, most quantum mechanical studies of crystalline solids are based on density functional theory, DFT, and the accuracy and limitations of this approach for the calculation of ground state properties are well known. The predictive power of DFT calculations with respect to the correct description of pressure induced structural changes in high symmetry compounds has recently been assessed and it was stressed, that calculations such as those used here are very reliable [17].

For the density functional theory based calculations employed here, the PBE-version of the generalized gradient-approximation, GGA, was employed. We used academic and commercial versions of the CASTEP program, which has been described elsewhere [18]. In these calculations, ultrasoft pseudopotentials from the CASTEP database were used with a maximum cutoff energy of the plane waves of 450 eV. In addition to the cutoff energy, one further parameter determines the quality of the calculations, namely the density of points with which the Brillouin zone is sampled. The wave vectors for the sampling points were chosen according to the scheme proposed by Monkhorst and Pack [19]. Here, we use a sampling of reciprocal space such that distances between grid points are less than $0.032\,\text{Å}^{-1}$. Full geometry optimization calculations were performed for $Y_2[Si_4N_6C]$ in which all structural parameters were relaxed simultaneously for 22 pressures between zero and 30 GPa. After the final self-consistency cycle the remaining stress was less than 0.05 GPa. The present calculations are restricted to the athermal limit, in which temperature effects and zero-point motions are neglected.

Due to the requirement of excessive computational resource the pressure dependence of the Ho- and Er-compounds could not be studied theoretically. The ground state geometry optimisation of $Ho_2[Si_4N_6C]$ took more than 380 h on a 16 cpu cluster, and hence an equation of state could not be computed on a reasonable time-scale.

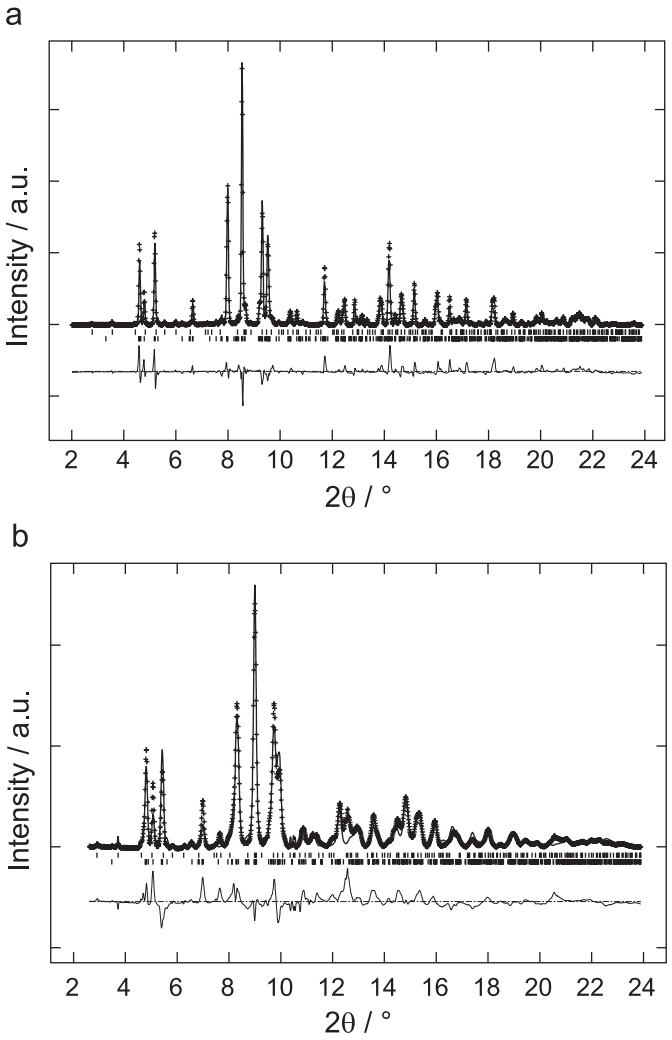

Fig. 2. Observed (+), calculated (line), and difference (at the bottom) X-ray powder diffraction profiles of $Ho_2[Si_4N_6C]$ after subtraction of the background using a Chebyshev function at (a) 0.0001 GPa and (b) 31.953(8) GPa. Vertical marks correspond to the positions of the Bragg reflections of $Ho_2[Si_4N_6C]$ (bottom) and $Ho_6[Si_{11}N_{20}O]$ (top).

2.4. Data analysis

Isothermal bulk moduli B_0, their pressure derivatives B', B'' and B''', and the volume at zero pressure V_0 were analyzed from fits of Birch-Murnaghan (BM) equations of state (EOS) [20] up to 5th order [21] to pressure-volume (pV) data applying EOS-FIT [22] and a general least-squares program [23]. The pressure volume data were weighted with the appropriately scaled experimental errors in pressure and volume. For weighting pV-data from the DFT calculations the maximal remaining stress in the calculations (0.05 GPa) was assumed to correspond to $3\sigma(p)$. Furthermore, the pV-data were transformed into Eulerian strain versus normalized stress fF-plots [24], in order to visualize complex trends of the compression behaviour which are not directly apparent from pV-plots.

The compression behaviour of a monoclinic structure under the influence of a hydrostatic stress state is fully described by the unit strain tensor. This tensor is of 2nd order and describes the deformation per GPa in an orthonormal basis system xyz chosen here with y parallel b and z parallel c of the monoclinic unit cell. The representation surface of the strain tensor is usually an ellipsoid that may be rotated within the monoclinic ac-plane. The magnitude and the orientation of the main axes of the strain ellipsoid were calculated from the cell parameters with the program STRAIN [25]. By definition, the magnitudes of the main axes of the strain ellipsoid for the lowest pressure studied are $|\varepsilon 3| > |\varepsilon 2| > |\varepsilon 1|$.

3. Results

3.1. Bulk compressibility

Unit cell parameters of $Ho_2[Si_4N_6C]$, $Er_2[Si_4N_6C]$ and $Y_2[Si_4N_6C]$ as a function of pressure are summarized in Tables 1, 2, and 3, respectively. The predicted unit-cell parameters of $Y_2[Si_4N_6C]$ at ambient conditions are compared to experimental data in Table 3.

They are larger by less than 2% compared to the experiment, which is usually observed in DFT-GGA calculations such as those performed here.

Unit-cell volumes and equations of state are plotted as a function of pressure in Fig. 3, the corresponding fit parameters are summarized in Table 4. The pV-data of $Y_2[Si_4N_6C]$ show an anomaly between around 8 and 12 GPa. This anomalous behaviour cannot be described by either a third-, fourth- or fifth-order BM-EOS. This becomes more clear comparing plots of the normalized pressure versus Eulerian strain (fF-plot), shown in Fig. 4.

If the data points in an fF-plot lie on a horizontal line of constant F then $B' = 4$, and the data can be fitted with a second-order BM-EOS. If the data lie on an inclined straight line, the data will be adequately described by a third-order BM-EOS. Positive or negative slopes imply $B' > 4$ and $B' < 4$, respectively. In all the cases, the intercept on the F-axis is the value of B_0 [24]. A curvature of the plot either suggests an EOS of higher order, the change of the compression mechanism or a structural phase transition.

The fF-plots of $Ho_2[Si_4N_6C]$ and $Er_2[Si_4N_6C]$ are well represented by a third-order BM-EOS (Fig. 4). We observe a deviation from the linear behaviour at small strains. This generally indicates a problem with the determination of the ambient pressure unit cell volume, V_0 [24], and indeed our fitted V_0 is smaller than the value obtained from our own and other [8] ambient pressure measurements. In summary, Table 4 and Fig. 4 show that the bulk compression behaviour of the Ho- and Er-carbidonitridosilicates is

Table 1
Pressure dependencies of the unit cell parameters of $Ho_2[Si_4N_6C]$.

p (GPa)	a (Å)	b (Å)	c (Å)	β (deg)	V (Å)^3
0*	5.9415	9.9966	11.9143	119.794	614.11
0.0001	5.934(2)	9.8999(6)	11.873(4)	119.714(7)	605.78(4)
0.370(3)	5.9241(9)	9.8843(5)	11.863(2)	119.692(5)	603.44(3)
1.058(8)	5.919(1)	9.8638(5)	11.846(3)	119.684(6)	600.85(4)
2.56(1)	5.908(1)	9.8255(6)	11.816(3)	119.665(6)	595.99(4)
3.651(5)	5.894(2)	9.7958(6)	11.801(4)	119.645(7)	592.19(5)
5.14(1)	5.882(2)	9.7613(6)	11.777(4)	119.621(6)	587.88(5)
6.88(2)	5.871(1)	9.7180(6)	11.736(3)	119.587(6)	582.29(5)
9.11(2)	5.853(1)	9.6720(7)	11.699(3)	119.560(7)	576.03(5)
11.52(1)	5.836(1)	9.6287(8)	11.650(2)	119.544(9)	569.57(6)
12.84(2)	5.826(1)	9.6073(9)	11.619(2)	119.56(1)	565.71(6)
15.476(8)	5.807(1)	9.5728(9)	11.570(2)	119.58(1)	559.40(6)
17.00(1)	5.795(1)	9.5491(9)	11.541(2)	119.57(1)	555.50(6)
19.665(8)	5.781(1)	9.514(1)	11.502(2)	119.54(1)	550.38(7)
22.96(2)	5.762(1)	9.469(1)	11.453(2)	119.56(2)	543.61(8)
25.260(8)	5.747(2)	9.424(1)	11.410(3)	119.51(2)	537.8(1)
28.05(1)	5.732(1)	9.407(1)	11.384(3)	119.49(2)	534.36(9)
29.37(1)	5.724(2)	9.379(1)	11.354(3)	119.47(2)	530.6(1)
31.953(8)	5.711(2)	9.358(1)	11.332(3)	119.47(2)	527.2(1)
35.83(6)	5.689(2)	9.309(1)	11.282(3)	119.43(2)	520.3(1)

Unit-cell parameters at 0 GPa from DFT calculations are marked with an asterisk.

Table 2
Pressure dependencies of the unit-cell parameters of $Er_2[Si_4N_6C]$.

p (GPa)	a (Å)	b (Å)	c (Å)	β (deg)	V (Å)^3
0.0001	5.9177(9)	9.8878(6)	11.857(2)	119.692(7)	602.70(5)
0.607(3)	5.914(1)	9.8678(6)	11.843(2)	119.684(7)	600.43(5)
2.406(6)	5.902(2)	9.8191(8)	11.808(5)	119.670(9)	594.63(6)
4.455(9)	5.877(1)	9.7624(7)	11.772(3)	119.585(7)	587.32(6)
6.89(2)	5.859(2)	9.6970(8)	11.721(5)	119.548(9)	579.32(7)
8.49(3)	5.856(2)	9.665(1)	11.697(5)	119.52(1)	576.05(9)
11.693(3)	5.837(1)	9.589(1)	11.629(3)	119.46(1)	566.78(9)
14.027(5)	5.816(1)	9.549(1)	11.571(3)	119.41(1)	559.82(9)
17.45(1)	5.793(1)	9.499(1)	11.507(2)	119.33(1)	552.06(9)
20.63(4)	5.774(1)	9.454(1)	11.457(2)	119.32(1)	545.4(1)

Table 3
Pressure dependencies of the unit-cell parameters of $Y_2[Si_4N_6C]$ from DFT calculations.

p (GPa)	a (Å)	b (Å)	c (Å)	β (deg)	V (Å)^3
0	6.0336	10.0604	12.0955	119.641	638.123
0.0001*	5.9295(1)	9.8957(1)	11.8800(2)	119.63(4)	605.92
1	6.0250	10.0297	12.0753	119.620	634.343
2	6.0160	10.0022	12.0567	119.610	630.749
3	6.0073	9.9737	12.0372	119.597	627.107
4	5.9962	9.9512	12.0213	119.613	623.610
5	5.9893	9.9234	12.0004	119.598	620.168
6	5.9771	9.9061	11.9800	119.640	616.514
7	5.9700	9.8804	11.9647	119.631	613.459
8	5.9590	9.8649	11.9411	119.676	609.885
9	5.9515	9.8398	11.9253	119.678	606.754
10	5.9404	9.8291	11.8993	119.775	603.062
11	5.9273	9.8190	11.8739	119.896	599.106
12	5.9164	9.8045	11.8508	119.980	595.453
13	5.9058	9.7902	11.8305	120.047	592.102
15	5.8870	9.7576	11.7957	120.109	586.154
16	5.8784	9.7398	11.7813	120.136	583.356
18	5.8604	9.7067	11.7527	120.168	578.005
20	5.8432	9.6748	11.7262	120.185	573.019
25	5.8035	9.5986	11.6655	120.215	561.545
28	5.7797	9.5560	11.6327	120.218	555.180
29	5.7725	9.5428	11.6220	120.225	553.174
30	5.7655	9.5288	11.6107	120.222	551.172

Experimental data at 0.0001 GPa are marked with an asterisk [7].

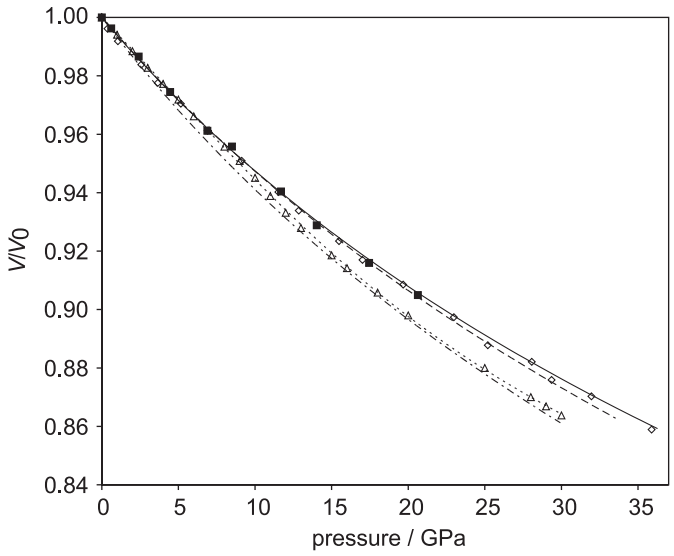

Fig. 3. Pressure dependence of the normalized unit cell volumes of $Ho_2[Si_4N_6C]$ (open diamonds), $Er_2[Si_4N_6C]$ (filled squares) and $Y_2[Si_4N_6C]$ (open triangles). Standard deviations are smaller than symbols. BM-EOS fits to data are shown for $Ho_2[Si_4N_6C]$ (3rd-order: solid line), $Er_2[Si_4N_6C]$ (3rd-order: dashed line) and $Y_2[Si_4N_6C]$ (3rd-order: chain dotted line; 4th-order: dotted line).

Table 4
Bulk compression parameters fitted with the Birch–Murnaghan equation of state BM-EOS.

Compound	Order of EOS	V_0 (Å^3)	B_0 (GPa)	B'	p_{max} (GPa)
$Ho_2[Si_4N_6C]$	Third	605.1(2)	162(2)	5.1(3)	36
$Er_2[Si_4N_6C]$	Third	602.8(2)	163(5)	4.5(6)	21
$Y_2[Si_4N_6C]$	From fF-plot	638.1	165	4	9

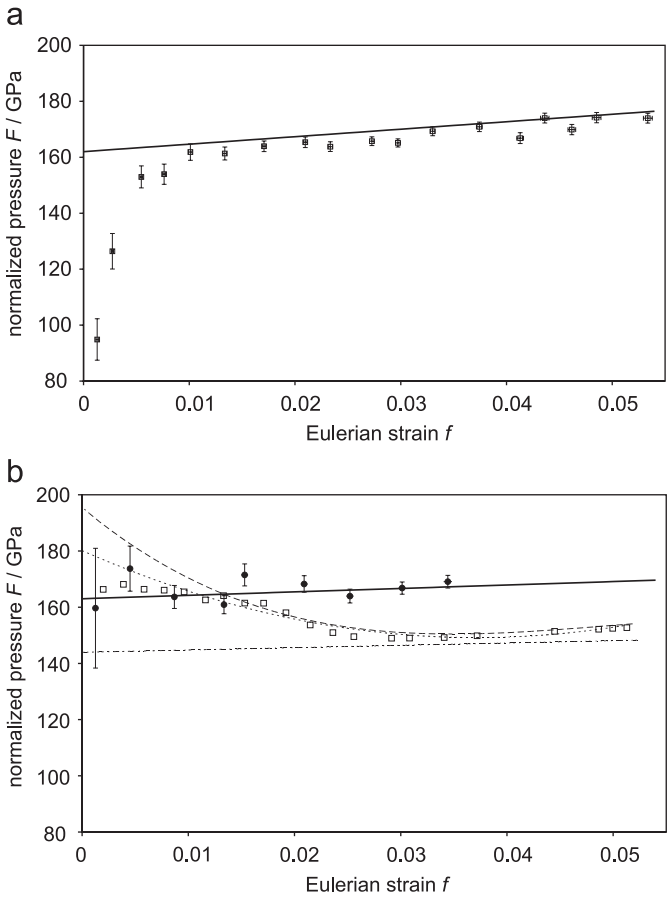

Fig. 4. The volume-pressure data as a plot of the normalized pressure F against the Eulerian strain f of (a) $Ho_2[Si_4N_6C]$ and (b) $Er_2[Si_4N_6C]$ (filled circles) and $Y_2[Si_4N_6C]$ (open squares). Third-order BM-EOS fits to the complete data sets are represented by straight lines, 4th- or 5th-order BM-EOS fits by curved lines. Clearly, in (b) the data points for $Er_2[Si_4N_6C]$ are well described by the solid line and hence a 3rd-order BM-EOS is appropriate, while for $Y_2[Si_4N_6C]$ neither a 3rd-, 4th- nor 5th-order BM-EOS (represented by the chain dotted, dotted, or dashed line, respectively) describes the data adequately.

essentially the same and the pressure dependence of the volume is well described by a 3rd order BM-EOS with the bulk modulus $B \approx 162$ GPa.

However, the fF-dependence of $Y_2[Si_4N_6C]$ cannot reasonably be described by a third-, fourth- or fifth-order BM-EOS. While the fit of a fourth-order BM-EOS to the pV-data seems to better describe the anomaly between 8 and 12 GPa (Fig. 3), the fF-plot shows that none of these EOSs is appropriate (Fig. 4). The fF-plot also shows that the bulk modulus $B_0 \approx 165$ GPa. This is similar to the values of the experimental data for $Ho_2[Si_4N_6C]$ with $B_0 = 162(2)$ GPa and $Er_2[Si_4N_6C]$ with $B_0 = 163(5)$ GPa.

3.2. Linear compressibility

Unit-cell parameters are plotted as a function of pressure in Figs. 5, 6, and 7 for $Ho_2[Si_4N_6C]$, $Er_2[Si_4N_6C]$, and $Y_2[Si_4N_6C]$, respectively. A significant anisotropy of the axial compression is observed in all of the three compounds with the b axis being most compressible.

At low pressures the a- and c-axes of all three compounds behave similarly on compression. Above ≈ 10 GPa there is a distinct difference in the compressibilities of the axes. However, due to the pseudosymmetry and the resulting significant peak overlap in the experimental data, an assignment of the a- and c-axes of $Ho_2[Si_4N_6C]$ and $Er_2[Si_4N_6C]$ is not unambiguously possible

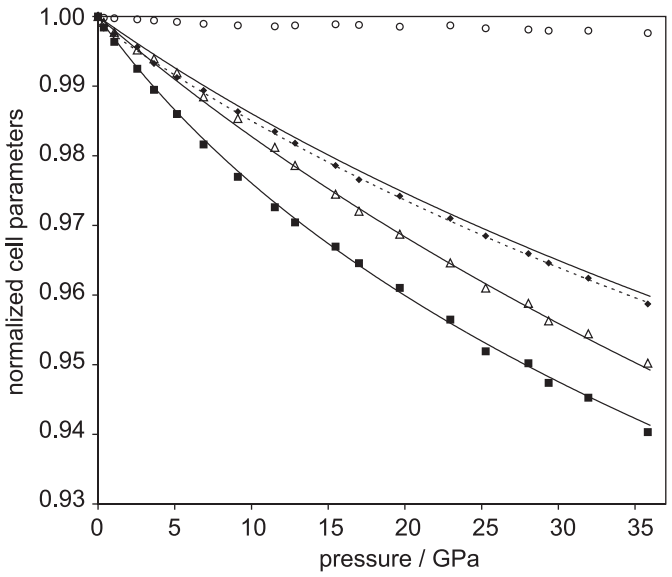

Fig. 5. Pressure dependencies of the normalized unit cell parameters of $Ho_2[Si_4N_6C]$. Symbols are drawn for a/a_0 (filled diamonds), b/b_0 (filled squares) and c/c_0 (open triangles) axes and β/β_0 (open circles). Symbols are larger than error bars. 3rd-order BM-EOS fits to the cell axes are represented by solid lines. In the fit a_0 is underestimated, which results in a line shift on normalization. Hence, the dotted line represents the EOS fit using the experimentally determined value for a_0 for normalization.

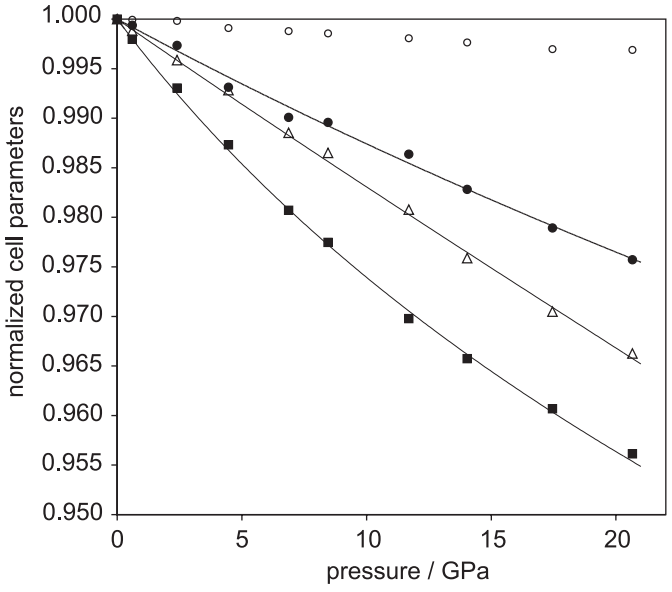

Fig. 6. Pressure dependencies of the normalized unit cell parameters of $Er_2[Si_4N_6C]$. Symbols are drawn for a/a_0 (filled circles), b/b_0 (filled squares) and c/c_0 (open triangles) axes and β/β_0 (open circles). Error bars are about the size of the symbols. 3rd-order BM-EOS fits to the cell axes are represented by solid lines.

at pressures above the anomaly and depends on the starting parameters. When we used the computed high-pressure structural model of $Y_2[Si_4N_6C]$ as a constraint to the refinements of the powder diffraction patterns of $Ho_2[Si_4N_6C]$ and $Er_2[Si_4N_6C]$, the a axis is identified as the least compressible direction at these higher pressures.

The largest compression in a monoclinic system is not necessarily along the crystallographic axes since the strain ellipsoid may be rotated about the monoclinic axis. Figs. 8, 9, and 10 show the pressure dependencies of the main

axes of the strain ellipsoid and the rotation of the ellipsoid within the monoclinic *ac*-plane for $Ho_2[Si_4N_6C]$, $Er_2[Si_4N_6C]$ and $Y_2[Si_4N_6C]$, respectively.

$Ho_2[Si_4N_6C]$ (Fig. 8) and $Er_2[Si_4N_6C]$ (Fig. 9) show a conventional compression behaviour. The ε-values are negative due to the compression of the unit cell. The largest strain $\varepsilon 3$ is observed parallel *b*. The pressure-dependence of $\varepsilon 1$ and $\varepsilon 2$ is negligible, while the significant slope of $\varepsilon 3$ is positive. This corresponds to a constant compression in the (a, c)-plane, while the (larger) compressibility perpendicular to this plane (parallel *b*) is decreasing. With increasing pressure the strain ellipsoids rotate about the crystallographic *b*-axis. Above 15 GPa the axes of the strain ellipsoid are aligned essentially parallel to the orthogonal axes of the crystal-physical coordinate system in $Ho_2[Si_4N_6C]$, while in $Er_2[Si_4N_6C]$ an angle of 2–3° remains between the axes of the strain ellipsoid and the crystal physical coordinate system at pressures >10 GPa. Since the monoclinic angle is almost 120° this behaviour may be indicative of a structural phase transition into an ortho-hexagonal (i.e., orthorhombic) structure. However, the powder diffraction data obtained here were of insufficient resolution to clarify if the structure remained pseudo-symmetric or transformed into the high symmetry.

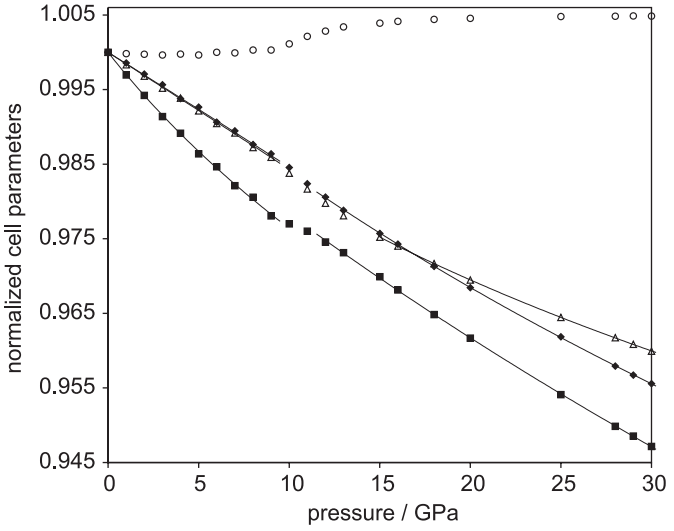

Fig. 7. Pressure dependencies of the normalized unit cell parameters of $Y_2[Si_4N_6C]$. Symbols are drawn for a/a_0 (filled diamonds), b/b_0 (filled squares) and c/c_0 (open triangles) axes and β/β_0 (open circles). 3rd-order BM-EOS fits to the cell axes from 0 to 8 GPa and from 12 to 30 GPa are represented by solid lines.

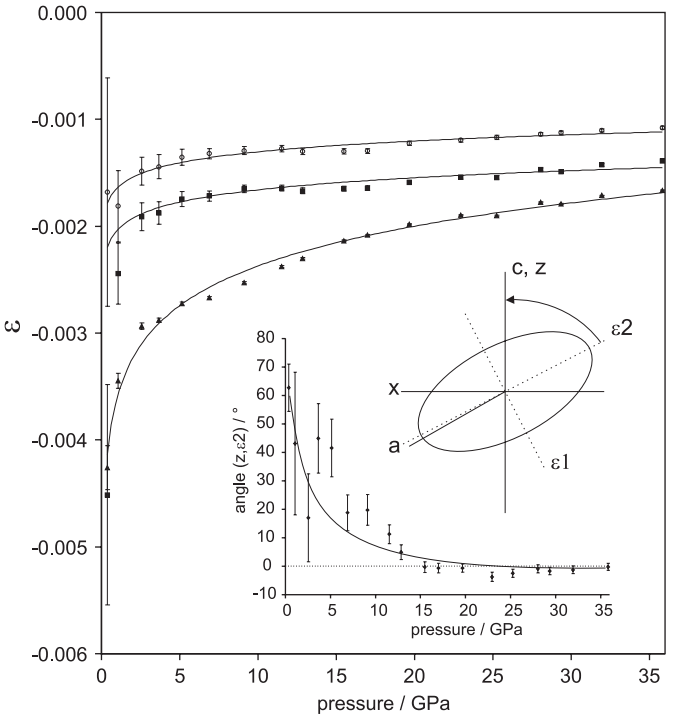

Fig. 8. Principal axes $\varepsilon 1$ (open circles), $\varepsilon 2$ (filled squares), and $\varepsilon 3$ (filled triangles) of the unit-strain ellipsoid of $Ho_2[Si_4N_6C]$ with pressure. Lines are guides to the eyes. The inset shows the orientation of the strain ellipsoid and the variation of the tilt angle between the *z* coordinate axis (equals crystallographic *c*-axis) and the $\varepsilon 2$ principal axis of the strain-tensor.

3.3. Structural compression mechanism of $Y_2[Si_4N_6C]$

The comparison of structural data of $Ho_2[Si_4N_6C]$ and $Y_2[Si_4N_6C]$ obtained from the DFT calculations to experimental

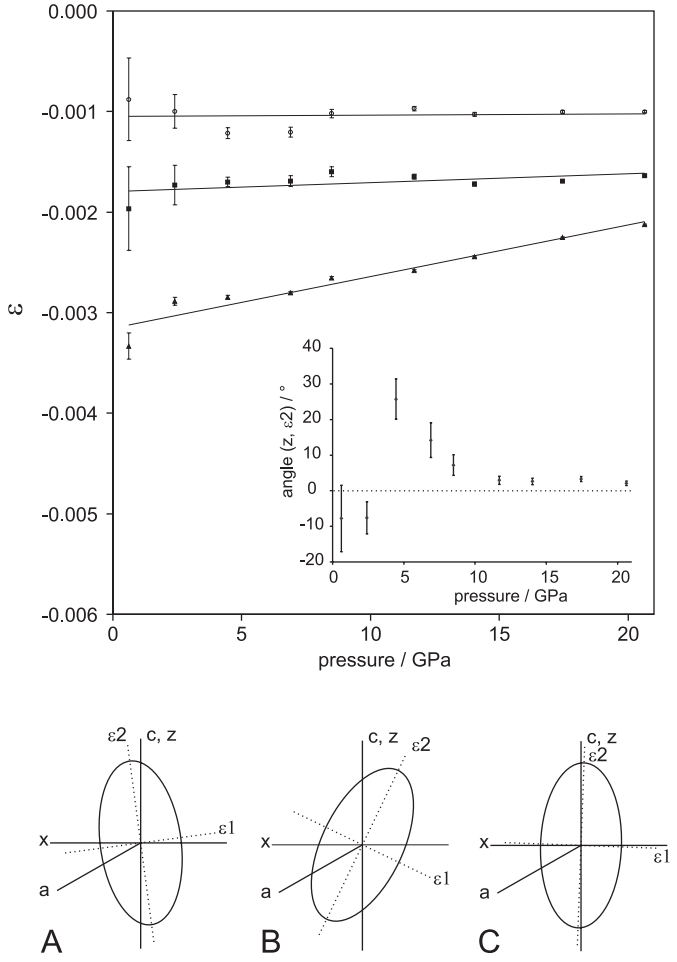

Fig. 9. Principal axes $\varepsilon 1$ (open circles), $\varepsilon 2$ (filled squares), and $\varepsilon 3$ (filled triangles) of the unit-strain ellipsoid of $Er_2[Si_4N_6C]$ with pressure. Lines are guides to the eyes. The inset shows the variation of the tilt angle between the *z* coordinate axis (equals crystallographic *c*-axis) and the $\varepsilon 2$ principal axis of the strain-tensor. Different rotational states of the strain ellipsoid at about 2, 4.5, and 20 GPa are indicated with the letters A,B and C, respectively.

data obtained by powder X-ray diffraction at ambient conditions [7,8] revealed no significant differences to the experimental data. This agreement is typical for state-of-the-art DFT calculations and hence we confidently predict the high pressure behaviour. Predicted fractional coordinates of $Ho_2[Si_4N_6C]$ at 0 GPa and of $Y_2[Si_4N_6C]$ at 0 and 30 GPa are given in Table 5.

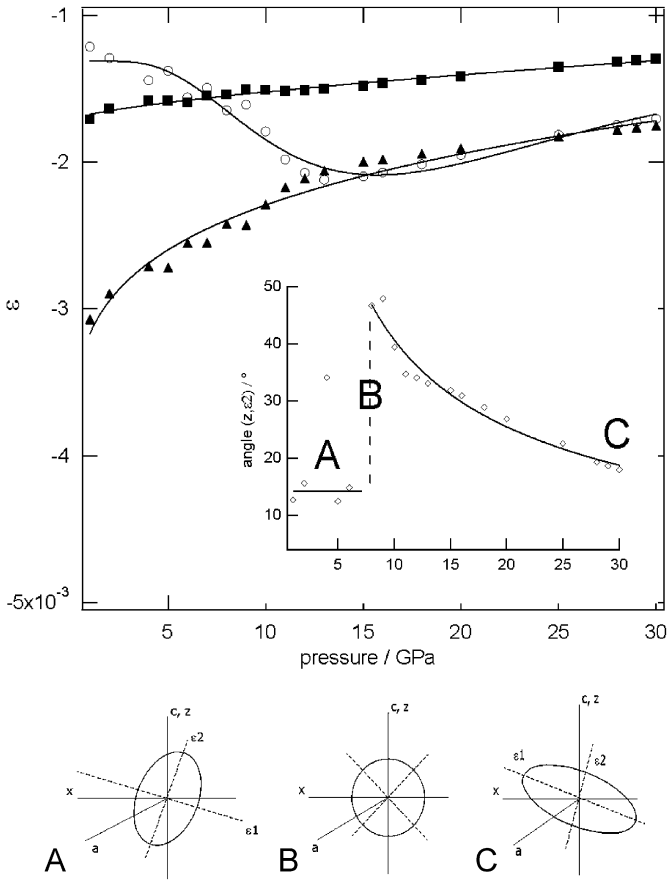

Fig. 10. Principal axes $\varepsilon 1$ (open circles), $\varepsilon 2$ (filled squares), and $\varepsilon 3$ (filled triangles) of the unit-strain ellipsoid of $Y_2[Si_4N_6C]$ with pressure. Lines are guides to the eyes. The inset shows the variation of the tilt angle between the z coordinate axis (equals crystallographic c-axis) and the $\varepsilon 2$ principal axis of the strain-tensor. Different rotational states of the strain ellipsoid at about 4, 8, and 30 GPa are indicated with the letters A, B and C, respectively.

The model calculations allow to investigate the compression mechanism, as they give the pressure-induced change of the detailed atomic arrangement. The structural compression of $Y_2[Si_4N_6C]$ is mainly achieved by a rotation and deformation of the SiN_3C tetrahedra. The most pronounced effects are observed in the pressure range between 8 and 12 GPa, where the anomalous pressure dependence of the unit-cell parameters occurs. The rotation is most noticeable by the change of some inter-tetrahedral Si–N–Si and Si–C–Si angles (Figs. 11 and 12). Since one of the Si–C bonds remains aligned parallel to the b axis the changes occur by deformations within the tetrahedral layer parallel to the ac-plane (Figs. 1 and 11).

The coupled tilting of the $Si(2)N_3C$ and $Si(3)N_3C$ tetrahedra is accompanied by a decrease of the Si1–C–Si3 angle (by about 5°) and the $Si_2-N_4-Si_4$ angle (by about 1.5°). Concomitantly, the Si1–C–Si2 and Si1–N3–Si3 angles increase by about 3° and 2°, respectively (Fig. 12). The displacement of the tetrahedra implies a decrease of the interstitial volumes, which are occupied by the large and compressible Y cations. Hence, it is not surprising, that in the pressure range between 8 and 12 GPa the coordination of the Y cations is increased. Changes in the coordination are due to a strong increase (e.g., Y1–N1, Y1–N6, Y2–N3) and decrease (e.g., Y1–N3) of interatomic distances, respectively (Fig. 13). At increasing pressure the coordination around Y1 is increased from [5 + 1] to [6 + 2] nitrogen atoms and around Y2 from [6] to [6 + 1] nitrogen atoms.

In the DFT-based structural model the Si1–C bond, which is oriented along the b-axis, is significantly shorter than the other Si–C bonds (Fig. 14). This is also observed in the experimentally determined structure of $Y_2[Si_4N_6C]$ [7]. Despite the difference in the lengths of the Si–C bonds, the magnitude of their compression is similar, and all are more compressible than the shorter Si–N bonds. It is interesting to note that pressure-induced continuous changes in the bond lengths and angles result in a discontinuous change in the orientation of the strain ellipsoid. It is also worthwhile to note that in the prediction the main axes of the strain ellipsoid in $Y_2[Si_4N_6C]$ do not align themselves with the axes of the crystal physical coordinate system.

4. Discussion

The experimentally determined bulk moduli are equal within one standard deviation and the effect of the Ho/Er substitution on the compressibility cannot be determined within the precision of

Table 5
Fractional atomic coordinates of $Ho_2[Si_4N_6C]$ at 0 GPa and of $Y_2[Si_4N_6C]$ at 0 and 30 GPa from DFT calculations.

	$Ho_2[Si_4N_6C]$, $p = 0$ GPa			$Y_2[Si_4N_6C]$, $p = 0$ GPa			$Y_2[Si_4N_6C]$, $p = 30$ GPa		
	x	y	z	x	y	z	x	y	z
Ho1/Y1	0.3239	0.5716	0.0916	0.3329	0.5650	0.0983	0.3498	0.5483	0.1169
Ho2/Y2	0.6525	0.4114	0.4169	0.6606	0.4131	0.4226	0.6970	0.4115	0.4480
Si1	0.0043	0.4793	0.2512	0.0051	0.4815	0.2518	0.0198	0.4771	0.2606
Si2	0.1616	0.2113	0.4204	0.1628	0.2109	0.4201	0.1691	0.1974	0.4218
Si3	0.1959	0.2067	0.1751	0.1938	0.2116	0.1745	0.1815	0.2262	0.1726
Si4	0.6749	0.2269	0.1588	0.6742	0.2301	0.1595	0.6699	0.2387	0.1657
N1	0.0281	0.2216	0.0083	0.0370	0.2271	0.0108	0.0225	0.2644	0.0105
N2	0.0619	0.0428	0.3985	0.0668	0.0445	0.3953	0.0885	0.0252	0.3950
N2	0.2371	0.0371	0.2185	0.2240	0.0420	0.2137	0.1694	0.0458	0.1790
N4	0.5007	0.2876	0.0009	0.4976	0.2873	0.0027	0.5090	0.2983	0.0067
N5	0.5150	0.2620	0.2445	0.5085	0.2655	0.2403	0.5027	0.2820	0.2460
N6	0.7008	0.0536	0.1369	0.7046	0.0577	0.1420	0.6746	0.0584	0.1531
C1	0.0210	0.2915	0.2535	0.0197	0.2942	0.2542	0.0231	0.2903	0.2642

Atoms are labelled according to Höppe et al. [8] and Zhang et al. [7], respectively.

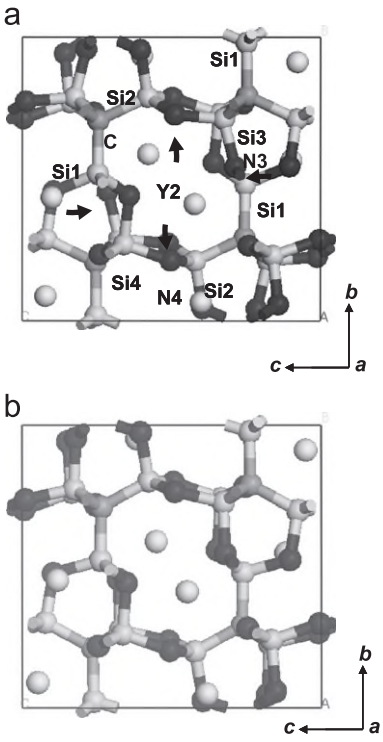

Fig. 11. Projection of the crystal structure of $Y_2[Si_4N_6C]$ along [1 0 0] at (a) 0 GPa and (b) 30 GPa. The sense of rotation of the $Si(3)N_3C$ tetrahedra is indicated by arrows in (a). Isolated spheres correspond to yttrium, light grey spheres to silicon, medium grey spheres to carbon, and dark grey spheres to nitrogen.

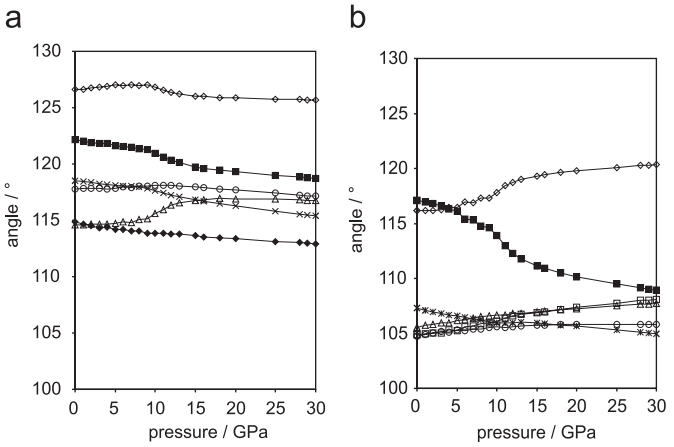

Fig. 12. Pressure dependencies of the (a) Si–N–Si angles and (b) Si–C–Si angles in $Y_2[Si_4N_6C]$.

our data (Table 4). The predicted bulk modulus and B' of $Y_2[Si_4N_6C]$ are also very similar to these values as can be derived from the *fF*-plot in Fig. 4.

The general deformation of framework structures can be analysed by studying the geometrical, topological and symmetrical properties of the framework. Possible deformations are determined by the rotation of the hinges connecting the tetrahedra, i.e. the C or N joints in the carbidonitridosilicates. In general frameworks can be rigid (inflexible) or flexible, where the latter can be grouped into collapsible and non-collapsible frameworks, depending on whether hinges are co- or antirotating [26]. The topology of the framework studied here does not allow

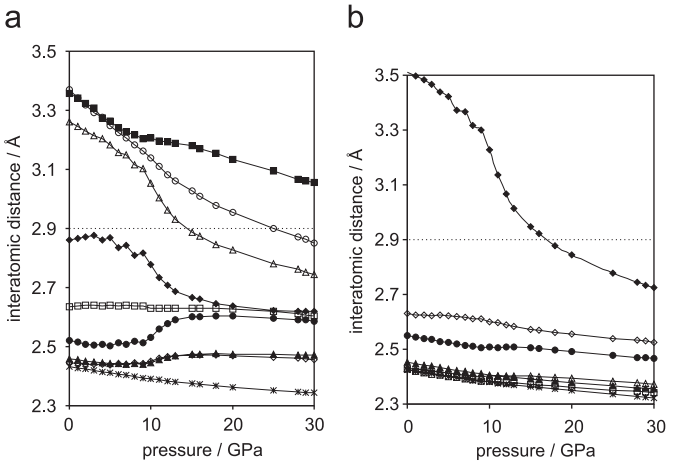

Fig. 13. Pressure dependencies of the (a) Y1–N bonds and (b) Y2–N bonds of $Y_2[Si_4N_6C]$. For the Y-coordinations an approximate cut-off distance of 2.9 Å as indicated by the dotted lines has to be assumed.

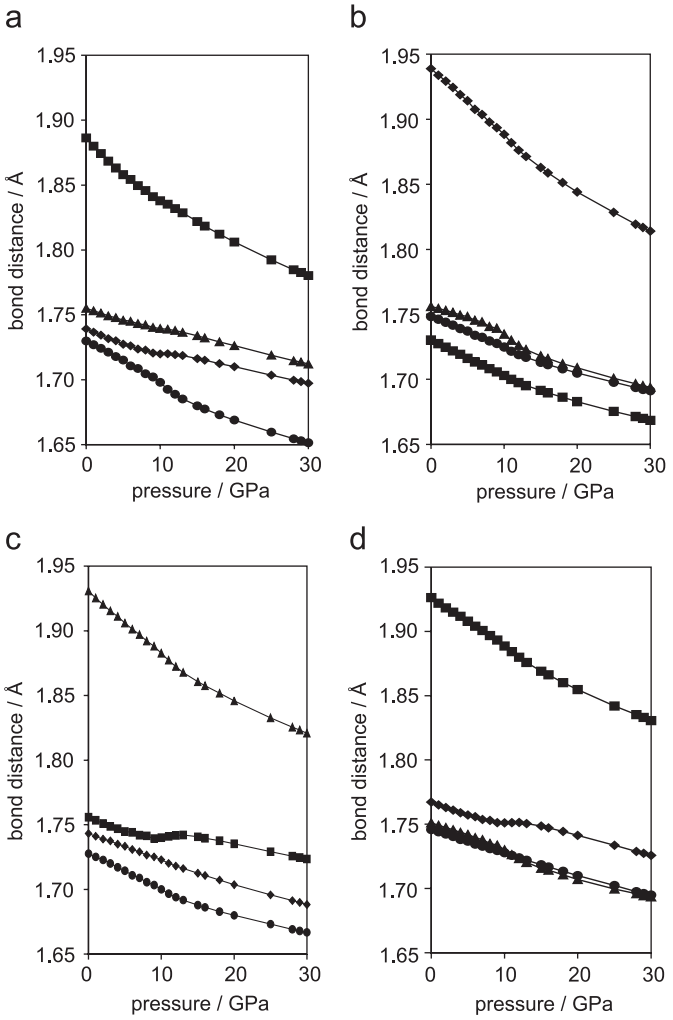

Fig. 14. Pressure dependencies of the Si–N and Si–C bonds of the coordination around (a) Si1, (b) Si2, (c) Si3, and (d) Si4 in $Y_2[Si_4N_6C]$. The Si–C bond is the longest and most compressible bond within each SiN_3C tetrahedron.

cooperative rotations in the (a,c)-plane. The reason is the linkage of three tetrahedra in the *ac*-layers (Fig. 1) by the single site tetrahedra within the chains along *b*. Assuming a

counter-clockwise rotation of the single site tetrahedra around *b*, the hinges connecting chains of star like units having the same alignment are frustrated and a possible cooperative tetrahedra deformation in the *ac* layers is blocked.

However, as our DFT calculations have shown, in monoclinic $Y_2[Si_4N_6C]$ the main pressure-induced structural changes are due to a tilting of tetrahedra in the (a, c)-layer which are caused by a deformation dominated by the shortening of the compressible Si–C bonds. Hence, the structures investigated here have a notable degree of flexibility. This is in contrast to the related compounds $SrYb[Si_4N_7]$ and the sialons $MYb[Si_2Al_2O_2N_5]$, where, due to their hexagonal symmetry and nearly hexagonal close-packed arrangement of the anions, such a tilting of the tetrahedra without changing the crystal symmetry is impossible. Consequently, the compression in these compounds can only be achieved by bond shortening. However, in contrast to what may be expected, this does not imply that the bulk moduli of the sialons are larger than those of the compounds investigated here. This is due to the role of structural building blocks, like the star-like units, and the presence or absence of four-fold coordinated C or N.

The experimentally determined bulk compressibilities of the structurally related sialons $SrYb[Si_{4-x}Al_xO_xN_{7-x}]$, $x = 2, (B_0 = 161(2)\,GPa)$ and $BaYb[Si_{4-x}Al_xO_xN_{7-x}]$, $x = 2, (B_0 = 168(2)\,GPa)$ are similar to those of the nitridocarbidosilicates ($B_0 \approx 163\,GPa$) [6]. In contrast, the nitridosilicate $SrYb[Si_4N_7]$ is less compressible with $B_0 = 176(2)\,GPa$ [6]. This correlates well with the lower compressibility of the Si–N bonds compared to the Si–C bonds (Fig. 14).

Hence, we conclude that the bulk compression seems to be mainly influenced by the structural motifs (chains of star-like units) and their framework-like connection, while a change in the cation coordination (which is different in the hexagonal and monoclinic structures) and of the stacking sequence of the chains (alternating in the nitridocarbidosilicates and parallel in the nitridosilicate and sialons) seem to play a minor role.

In contrast, a comparison to the predicted bulk moduli of the oxonitridoaluminosilicate $SrSiAl_2O_3N_2$ ($B_0 = 131.9(3)\,GPa$) and the oxonitridosilicate oxide $Ce_4[Si_4O_4N_6]O$ ($B_0 = 131(2)\,GPa$, $B' = 5.0(2)$), [27], as well as with the experimentally determined bulk modulus of oxonitridosilicate chloride $Ce_4[Si_4O_{3+x}N_{7-x}]Cl_{1-x}O_x$, $x \approx 0.2$ ($B_0 = 124(5)\,GPa$, $B' = 5(1)$), Friedrich et al. [28] shows, that those crystal-chemically related structures, which exhibit only $O^{[2]}$ and $N^{[2]}$ links instead of $N^{[4]}$ or $C^{[4]}$ links, are much more compressible, again emphasizing the role of the star-like units.

From a more generalised point of view the nitridocarbidosilicates and structurally related nitridosilicates and sialons can be described as host-guest materials based on covalently bound tetrahedrons (host) and large cations in the interstices (guests). Compressibility measurements on typical host-guest structures have revealed different tendencies. For silicon clathrates it has been found that the structural compression is mainly determined by the host structure and that the bulk modulus is only weakly dependent on the guests [29]. This is the case in our study as well. In contrast, it was found for zeolites that the host structure determines the main deformation mechanism, the compressibility however is controlled by the guests in isotypic zeolites [30,31]. Hence, it seems that the guests only weakly influence the compressibility of host-guest structures, which mainly compress by bond shortening (e.g., silicon clathrates and nitridocarbidosilicates), while a stronger influence of the guests is assumed for structures that allow polyhedral tiliting, with the guests determining the degree of polyhedral tilting (e.g., zeolites). We conclude that compressibility measurements seem to be a useful approach to quantify the strength of the interaction between the extra-framework components and the host by determining the change in compressibility upon substitution. However, the available data base is too small to establish such correlations at the moment.

5. Conclusions

We have shown that the monoclinic nitridocarbidosilicates $Ln_2[Si_4N_6C]$, Ln = Ho, Er, are stable up to at least 36 and 21 GPa, respectively. The bulk compression seems to be mainly influenced by the framework-like connection of star-like units, where carbon is [4]-coordinated by silicon. This conclusion is strengthened by the similar compressibilities of the structurally related hexagonal nitridosilicate $SrYb[Si_4N_7]$ and sialons $MYb[Si_{4-x}Al_xO_xN_{7-x}]$ ($x = 2$; M = Sr, Ba). We have further obtained detailed information on the structural compression of nitridocarbidosilicates from our DFT calculations on isotypic $Y_2[Si_4N_6C]$. While the computed compressibility is similar up to about 8 GPa, a distinct change in the structural compression was observed in the pressure range between 9 and 12 GPa. Whether such an anomaly also occurs in the compounds $Ln_2[Si_4N_6C]$ with Ln = Ho, Er cannot be determined unambiguously from our experimental powder X-ray diffraction data.

Acknowledgements

The authors gratefully acknowledge financial support from the Deutsche Forschungsgemeinschaft (DFG) through two grants (WI 1232/17-1 and SCHN 377/9) within the project SPP-1136 and through three grants (WI 1232/25-1, KN 507/5–1, and SCHN 377/13-1) within the project SPP-1236, and from the Fonds der Chemischen Industrie, Germany. Thanks are due to the ESRF for synchrotron beam time and financial support, and to S. Neidhart for help during the measurements.

References

[1] A. Zerr, G. Miehe, G. Serghiou, M. Schwarz, E. Kroke, R. Riedel, H. Fueß, P. Kroll, R. Boehler, Nature 400 (1999) 340.
[2] H. Huppertz, W. Schnick, Angewandte Chemie International Edition in English 35 (1996) 1983.
[3] H.A. Höppe, H. Lutz, P. Morys, W. Schnick, A. Seilmeier, Journal of Physics and Chemistry of Solids 61 (2000) 2001.
[4] R. Mueller-Mach, G. Mueller, M.R. Krames, H.A. Höppe, F. Stadler, W. Schnick, T. Juestel, P. Schmidt, Physica Status Solidi (a) 202 (2005) 1727.
[5] R.B. Kaner, J.J. Gilman, S.H. Tolbert, Science 308 (2005) 1268.
[6] E.A. Juarez-Arellano, A. Friedrich, K. Knorr, A. Lieb, B. Winkler, M. Amboage, M. Hanfland, W. Schnick, Acta Crystallographica B 62 (2006) 424.
[7] H.-C. Zhang, T. Horikawa, K.-I. Machida, Journal of the Electrochemical Society 153 (2006) H151.
[8] H.A. Höppe, G. Kotzyba, R. Pöttgen, W. Schnick, Journal of Materials Chemistry 11 (2001) 3300.
[9] R.D. Shannon, Acta Crystallographica A 32 (1976) 751.
[10] M. Valldor, M. Andersson, Solid State Sciences 4 (2002) 923.
[11] K. Liddell, D.P. Thompson, S.J. Teat, Journal of the European Ceramic Society 25 (2005) 49.
[12] M. Woike, W. Jeitschko, Journal of Solid State Chemistry 129 (1997) 312.
[13] H. Mao, P. Bell, J. Shaner, D. Steinberg, Journal of Applied Physics 49 (1978) 3276.
[14] A.P. Hammersley, S.O. Svensson, M. Hanfland, A.N. Fitch, D. Hausermann, High Pressure Research 14 (1996) 235.
[15] K. Syassen, DATLAB, Version 1.37d, MPI/FKF Stuttgart, Germany, 2005.
[16] A.C. Larson, R.B. Von Dreele, GSAS, Los Alamos National Laboratory Report LAUR, 1994, pp. 86–748.
[17] A. Mujica, A. Rubio, A. Munoz, R.J. Needs, Review of Modern Physics 75 (2003) 863.
[18] M.D. Segall, P.J.D. Lindan, M.J. Probert, C.J. Pickard, P.J. Hasnip, S.J. Clark, M.C. Payne, Journal of Physics: Condensed Matter 14 (11) (2002) 2717.
[19] H.J. Monkhorst, J.D. Pack, Physical Review B 13 (1976) 5188.
[20] F. Birch, Journal of Geophysical Research 83 (1978) 1257.
[21] A. Strachan, T. Cagin, W. Goddard III, Physical Review B 60 (22) (1999) 15083.
[22] R.J. Angel, EosFit5.2, 2001.

[23] T. William, C. Kelley, Gnuplot 4.0, 1986–1993, 1998, 2004.
[24] R.J. Angel, Equations of state, in: R. Hazen, R. Downs (Eds.), High-temperature and High-pressure Crystal Chemistry, Reviews in Mineralogy and Geochemistry, vol. 41, 2000, pp. 35–59.
[25] R. Hazen, L. Finger, A program to calulate the strain tensor from two sets of unit-cell parameters, in: Comparative Crystal Chemistry, Wiley, Chichester, 1982, pp. 92–102 (program written by Y. Ohashi).
[26] H. Bauer, Journal of Solid State Chemistry 97 (1992) 243.
[27] B. Winkler, M. Hytha, U. Hantsch, V. Milman, Chemical Physics Letters 343 (2001) 622.
[28] A. Friedrich, K. Knorr, A. Lieb, S. Rath, M. Hanfland, B. Winkler, W. Schnick, Z. Kristallogr. 220 (2005) 245.
[29] A. San-Miguel, P. Mélinon, D. Connétable, X. Blase, F. Tournus, E. Reny, S. Yamanaka, J. Itié, Physical Review B 65 (2002) 054109.
[30] G.D. Gatta, European Journal of Mineralogy 17 (2005) 411.
[31] G.D. Gatta, Z. Kristallogr. 223 (2008) 160.